Mon. Not. R. Astron. Soc. **000**, 1–18 (2015) Printed 25 March 2015 (MN LATEX style file v2.2)

Homogeneity and isotropy in the 2MASS Photometric Redshift catalogue

D. Alonso[1]*, A. I. Salvador[2], F. J. Sánchez[3], M. Bilicki[4,5], J. García-Bellido[2], E. Sánchez[3]

[1] *University of Oxford, Denys Wilkinson Building, Keble Road, Oxford, OX1 3RH, UK*
[2] *Instituto de Física Teórica, UAM-CSIC, Madrid, Spain.*
[3] *Centro de Investigaciones Energéticas Medioambientales y Tecnológicas, CIEMAT, Madrid, Spain.*
[4] *Astrophysics, Cosmology and Gravity Centre (ACGC), Department of Astronomy, University of Cape Town, South Africa.*
[5] *Kepler Institute of Astronomy, University of Zielona Góra, Poland.*

arXiv:1412.5151v2 [astro-ph.CO] 24 Mar 2015

25 March 2015

ABSTRACT

Using the 2MASS Photometric Redshift catalogue we perform a number of statistical tests aimed at detecting possible departures from statistical homogeneity and isotropy in the large-scale structure of the Universe. Making use of the angular homogeneity index, an observable proposed in a previous publication, as well as studying the scaling of the angular clustering and number counts with magnitude limit, we place constraints on the fractal nature of the galaxy distribution. We find that the statistical properties of our sample are in excellent agreement with the standard cosmological model, and that it reaches the homogeneous regime significantly faster than a class of fractal models with dimensions $D < 2.75$. As part of our search for systematic effects, we also study the presence of hemispherical asymmetries in our data, finding no significant deviation beyond those allowed by the concordance model.

Key words: cosmology: large-scale structure of the Universe – cosmology: observations

1 INTRODUCTION

In the last decades, due to the increasing abundance and quality of astronomical observations, we have been able to draw a fairly complete picture of the Universe on cosmological scales. The so-called ΛCDM (Λ - Cold Dark Matter) model can successfully explain the vast majority of observational data, and we are now able to constrain the value of many of its free parameters to percent precision (Planck Collaboration et al. 2014a). This model is based on a small number of premises, arguably the most fundamental of which is the Cosmological Principle (CP), which states that on large scales the distribution of matter in the Universe is homogeneous and isotropic.

The exact validity of the CP is unfortunately difficult to verify. While the high degree of isotropy of the Cosmic Microwave Background (CMB) (Fixsen et al. 1996; Planck Collaboration et al. 2014b) certainly supports this assumption in the early Universe, as well as during most of its history, it is not possible to unequivocally relate that to the degree of homogeneity of the present-day Universe[1].

Large-scale homogeneity and isotropy are usually taken for granted without proof in the application of many cosmological probes (Durrer 2011). This is often a reasonable approach, as long as the assumptions that go into the analysis methods are clearly stated and understood. However, since multiple cosmological observables rely on the validity of the CP, it would be desirable to verify these assumptions independently. Since the standard cosmological model allows for the presence of small-scale inhomogeneities, and it only approaches the ideal CP asymptotically on large scales, it is necessary to quantify the departure from the ΛCDM prediction as a function of scale. In the late-time Universe this can be done by studying the fractality of the galaxy distribution: in a pure fractal distribution, structures are found with the same amplitude on arbitrarily large scales, and homogeneity is never reached. The reader is referred to Martínez & Saar (2002), and references therein, for a thorough introduction to the theory of fractal point processes.

* E-mail: david.alonso@astro.ox.ac.uk

[1] It is worth noting that the late-time, non-linear evolution of density perturbations can potentially affect the background expansion of the Universe in a process called "back-reaction" (Räsänen 2011). However, since general back-reaction models preserve statistical homogeneity and isotropy, they cannot be constrained by our analysis.

Fractal dimensions quantify different moments of the counts-in-spheres in a point distribution. The most commonly used of them is the so-called correlation dimension $D_2(r)$, which quantifies the filling factor of spheres of different radii centred on points in the distribution. Using this kind of observables, different groups have been able to measure the transition from a fractal with $D_2 < 3$ to a homogeneous distribution $D_2 = 3$ on scales $r_H \sim 100\,\mathrm{Mpc}$ (Guzzo 1997; Pan & Coles 2000; Kurokawa et al. 2001; Hogg et al. 2005; Seshadri 2005; Sarkar et al. 2009; Scrimgeour et al. 2012; Nadathur 2013), while other authors claim that such transition has not yet been observed (Joyce et al. 1999, 2005; Sylos Labini 2011a,b; Sylos Labini et al. 2014). In order to perform such analyses, full three-dimensional information for all the galaxies is necessary, and therefore these methods have only been used on spectroscopic catalogues, which traditionally cover much smaller volumes than their photometric counterparts. As we however showed in a previous publication (Alonso et al. 2014), it is possible to adapt this kind of study to 2-dimensional data projected on the celestial sphere and still be able extract information regarding the fractality of the local large-scale structure. This method can be combined with the traditional analysis of the scaling of the 1- and 2-point statistics of the galaxy distribution with magnitude limit to study the effective fractal dimension of the galaxy distribution using only angular information. With extra radial information, such as photometric redshifts, the constraints on possible departures from the CP can be enhanced further.

In this work we apply these techniques to the 2MASS Photometric Redshift catalogue (2MPZ, Bilicki et al. 2014), an almost full-sky dataset providing comprehensive information on the galaxy distribution in the local Universe ($\bar{z} \sim 0.1$). We are thus able to study possible departures from the CP on very large angular scales at late times, when these departures are expected to be maximal. The paper is structured as follows: in Section 2 we present the methods and observables implemented on our data, as well as the ΛCDM predictions for these observables. Section 3 gives an overview of the 2MPZ catalogue, the sample used in this work and the criteria used in its selection. Section 4 presents our results regarding the fractality of the galaxy distribution in our sample. In Section 4.3 we study the impact of different potential sources systematics that could affect our results. In particular we investigate the presence of hemispherical asymmetries in our final sample. Finally Section 5 summarizes our results. We also present, in Appendices A and B, the methods to generate mock ΛCDM and fractal realizations of the galaxy distribution that were used in this analysis.

2 TESTS OF HOMOGENEITY USING ANGULAR INFORMATION

Often in optical and near-infrared galaxy surveys it is not possible to measure precise redshifts for every object, mainly due to the large amount of time needed to integrate down the noise in a narrow-band spectrograph. Complete spectroscopic samples are thus typically shallower than photometric ones, reaching the shot noise limit faster. The situation is particularly striking in the context of *all-sky* (4π sterad) galaxy surveys. While the largest photometric catalogues covering the whole celestial sphere (optical SuperCOSMOS, infrared 2MASS and WISE) include hundreds of millions of sources, their largest spectroscopic counterpart, the 2MASS Redshift Survey (Huchra et al. 2012), contains only 45,000 galaxies, hardly reaching beyond $z = 0.05$. Deep all-sky catalogues are however essential if one desires to test the isotropy in matter distribution, and certainly favourable also for studying its homogeneity.

If large volumes or number densities are needed for a particular study, it is often necessary to use datasets containing only angular coordinates and measured fluxes in a few wide bands for each object. Although this severely constrains the range of analyses that can be performed on these catalogues, there is still a great deal of cosmological information that can be extracted. In this Section we will describe different studies, related to the degree of homogeneity of the galaxy distribution, which can be performed using only angular information, starting with a brief review of angular clustering statistics.

2.1 Angular clustering

Probably the most informative observable regarding the statistics of the projected galaxy distribution is the angular two-point correlation function $w(\theta)$, defined as the excess probability of finding two galaxies with an angular separation θ with respect to an isotropic distribution

$$dP(\theta) = \bar{n}_\Omega^2\,[1 + w(\theta)]\;d\Omega_1\,d\Omega_2, \tag{1}$$

where $\bar{n}_\Omega$ is the mean angular number density of galaxies.

The modelling of $w(\theta)$ has been extensively covered in the literature (Peebles 1980; Crocce et al. 2011) and we will only quote the main results here. The angular density of galaxies can be expanded in terms of its harmonic coefficients a_{lm}, which for a statistically isotropic distribution are uncorrelated and described by their angular power spectrum $C_l \equiv \langle |a_{lm}|^2 \rangle$. The C_l are straightforwardly related to $P_0(k)$, the 3D power spectrum at $z = 0$:

$$C_l = \frac{2}{\pi}\int_0^\infty dk\,k^2\,P_0(k)|\omega_l(k)|^2, \tag{2}$$

where

$$\omega_l(k) \equiv \int_0^\infty d\chi\,\chi^2\,W(\chi)\,G(z)\,[b(z)j_l(k\chi) - f(z)j_l''(k\chi)] \tag{3}$$

Here $b(z)$ is the galaxy bias, χ is the radial comoving distance, related to the redshift in a homogeneous background through

$$\chi(z) = \int_0^z \frac{c\,dz}{H(z)}, \tag{4}$$

$j_l(x)$ is the $l-$th order spherical Bessel function and $G(z)$ and $f(z)$ are the linear growth factor and growth rate respectively (implicitly functions of the comoving distance χ on the lightcone). The quantity $W(\chi)$ above is the survey selection function, describing the average number density of sources as a function of the comoving distance to the observer and normalized to

$$\int_0^\infty W(\chi)\,\chi^2\,d\chi = 1. \tag{5}$$

Finally, the angular power spectrum is related to the angular correlation function through an expansion in Legendre polynomials L_l

$$w(\theta) = \sum_{l=0}^{\infty} \frac{2l+1}{4\pi} C_l \, L_l(\cos\theta). \quad (6)$$

For small angular separations it is possible to use the so-called Limber approximation (Limber 1953), which simplifies the relations above:

$$C_l = \int_0^{\infty} d\chi \, [\chi \, W(\chi) \, b(z) \, G(z)]^2 \, P\left(k = \frac{l+1/2}{\chi}\right), \quad (7)$$

$$w(\theta) = \int_0^2 d\chi \, \chi^4 \, W^2(\chi) \int_{-\infty}^{\infty} d\pi \, \xi\left(\sqrt{\pi^2 + \chi^2\theta^2}\right), \quad (8)$$

where $\xi(r)$ is the three-dimensional correlation function, and π is the radial separation between two galaxies.

2.2 The angular homogeneity index

In a three-dimensional framework, one of the most commonly used observables to describe the fractality of a point distribution is the so-called correlation dimension. Let us first define the correlation integral $C_2(r)$ as the average number of points contained by spheres of radius r centred on other points of the distribution. For an infinite homogeneous point process this quantity would grow like the volume $C_2(r) \propto r^3$. The correlation dimension is thus defined as the logarithmic tilt of the correlation integral:

$$D_2(r) \equiv \frac{d \log C_2}{d \log r}, \quad (9)$$

and hence, if the point distribution is uncorrelated on large scales, $D_2(r)$ should approach 3 for large r. In a FRW universe we can expect deviations from this value due to the gravitational clustering of density perturbations[2], but the homogeneous result should be approached asymptotically on large scales according to the Cosmological Principle. See Bagla et al. (2007); Yadav et al. (2010) for a thorough modelling of these quantities within the standard cosmological model.

In our case, due to the lack of precise radial information, we will use instead the angular homogeneity index $H_2(\theta)$, defined in Alonso et al. (2014) by directly adapting the definitions of C_2 and D_2 to a 2-dimensional spherical space. That is, we define the angular correlation integral $G_2(\theta)$ as the average counts of objects in spherical caps (instead of spheres), and the angular homogeneity index $H_2(\theta)$ as the tilt of G_2 with the area of these spherical caps $V(\theta) \equiv 2\pi(1-\cos\theta)$. Thus H_2 is normalized to be 1 for an infinite homogeneous distribution, and in a FRW universe it can be related to the angular correlation function (to first order) via

$$H_2(\theta) = 1 - \frac{\bar{w}(\theta) - w(\theta)}{1 + \bar{w}(\theta)} - \frac{1}{2\pi\bar{n}_\Omega \, (1-\cos\theta)}, \quad (10)$$

where

$$\bar{w}(\theta) \equiv \frac{1}{1-\cos\theta} \int_0^{\theta} w(\theta) \sin\theta \, d\theta. \quad (11)$$

[2] The finiteness of the point distribution will also cause deviations from homogeneity due to shot noise. This can be fully incorporated in the modelling of D_2 and $H_2(\theta)$. See Alonso et al. (2014) for further details.

We elaborate further on the technical details regarding the estimation of the angular homogeneity index from a galaxy survey and how to deal with boundary effects in Section 4.2. These are also more thoroughly discussed in Alonso et al. (2014), and we refer the reader to that paper for further information.

One may think that the net effect of using only angular information directly translates in a decrease of sensitivity, but this is not necessarily the case, especially when the aim is to provide model-independent constraints. Using only angular, and therefore observable information has the advantage that no assumption about the underlying cosmological model is necessary in order to convert redshifts into distances. This therefore allows for a cleaner test of homogeneity. Other probes, although more sensitive a priori, are ultimately a consistency test of some classes of cosmological models.

2.3 Scaling relations

As pointed out by Peebles (1993), a lot of information regarding the degree of homogeneity of the galaxy distribution can be extracted from the scaling of different observables with the limiting flux for a magnitude-limited survey. Given the sample's luminosity function $\phi(L, z)$, describing the number density of galaxies in an interval dL of luminosity at redshift z, a survey with a limiting flux F_c should observe a number density of galaxies as a function of distance χ given by

$$\bar{n}(\chi, > F_c) = \int_{L_{\rm min}}^{\infty} \phi(L, z(\chi)) dL, \quad (12)$$

where $L_{\rm min} = 4\pi \, F_c \, d_L^2(\chi)$ is the limiting luminosity at a distance χ and d_L is the luminosity distance. For low redshifts we can approximate $d_L \sim \chi$, and hence, for a non-evolving population ($\phi(L, z) \equiv \phi(L)$) we obtain that the number density should be purely a function of the combination $\sqrt{F_c}\chi$:

$$\bar{n}(\chi, > F_c) \equiv g(x \equiv \sqrt{F_c}\chi) = \int_{4\pi x^2}^{\infty} \phi(L) \, dL. \quad (13)$$

Without any redshift information we will actually observe the projected number density of galaxies, defined as the number of galaxies observed per unit solid angle:

$$\bar{n}_\Omega(> F_c) = \int_0^{\infty} \bar{n}(\chi, > F_c) \, \chi^2 \, d\chi, \quad (14)$$

from which it is easy to extract the scaling law:

$$\bar{n}_\Omega(> F_c) \propto F_c^{-3/2} \propto 10^{\beta \, m_{\rm lim}}, \quad (15)$$

where $m_{\rm lim}$ is the apparent magnitude limit and $\beta = 0.6$. Although it is not easy to assess the expected observational uncertainty on β, as shown in Peebles (1993), fractal models would predict a much smaller value. In particular it is easy to prove that for a model with a fractal dimension D, in which number counts follow the law $N \propto R^D$, we would measure $\beta \sim 0.2 \, D$.

An even stronger relation can be found for the two-point angular correlation function. Using Eq. 8 and the fact that $W(\chi) \propto \bar{n}(\chi, > F_c)$, it is straightforward to show that for two different flux cuts F_1 and F_2 the corresponding correlation functions would be related by

$$w_2(\theta) = \frac{w_1(B\theta)}{B}, \quad (16)$$

where the scaling factor B is[3] $B \sim \sqrt{F_1/F_2}$.

This is a well known result: as we increase the depth of the survey, we increase the chance that pairs of galaxies that are distant from each other (and therefore uncorrelated) will subtend small angles, thus decreasing the amplitude of the angular correlation function. Traditionally the scaling relation above has been used as a tool to rule out systematic errors associated with incorrect angular masking, however it can also be used as a consistency check to verify the statistical homogeneity of the galaxy distribution.

The reason for this can be understood intuitively. Consider a perfect fractal distribution, for which structures are found on all scales with the same amplitude. As we increase the survey depth, we will also include larger and larger structures, an effect which compensates for the loss of correlation described above. The result is that for a scale-independent fractal, the angular correlation function is independent of the survey depth, and hence of the magnitude limit (see Peebles 1993 for a precise derivation of this result in the case of Rayleigh-Levy flights). This test complements the calculation of the angular homogeneity index, described in the next Section, in that it is able to probe the degree of homogeneity also in the radial direction.

Although the measurement of these scaling relations is an important test of homogeneity and isotropy, these analysis suffer from a number of caveats that must be highlighted. First of all, assuming a non-evolving luminosity function is not necessarily correct for all galaxy populations, and could induce a bias in our measurement of β. Secondly, while nothing prevents us from computing the two-point correlation function in an inhomogeneous dataset, its interpretation in terms of an excess probability of finding pairs of galaxies is only valid in the homogeneous case. Because of this, the study of the scaling relations should be undestood as a consistency test of the homogeneous model, and not as a model-independent constraint on inhomogeneous cosmologies. Finally, it is worth noting that the exact form of the scaling relations presented here should vary in deeper catalogues reaching larger redshifts, which will be a concern for future surveys. This is, however, not a issue for 2MPZ, where $\bar{z} \sim 0.1$.

3 THE DATA

3.1 The 2MASS Photometric Redshift catalogue

The 2MASS Photometric Redshift catalogue (2MPZ, Bilicki et al. 2014) is the first publicly available[4] all-sky dataset that provides photometric redshift information. Its parent sample, the 2MASS Extended Source Catalogue (XSC, Jarrett et al. 2000) includes over 1.6 million resolved sources (mostly galaxies), detected on most of the sky except for the highly confused Galactic Bulge, and provides precise astro- and photometric information, the latter in three near-infrared (IR) bands, J, H and K_s. About 1 million of the 2MASS galaxies are within its approximate completeness limit of $K_s \lesssim 13.9$ mag (Vega). By cross-matching the 2MASS XSC sample with two other major all-sky photometric surveys (deeper than 2MASS), SuperCOSMOS scans of photographic plates (Hambly et al. 2001) and mid-IR satellite data from WISE (Wright et al. 2010), Bilicki et al. (2014) obtained multiwavelength information for the majority (95%) of 2MASS galaxies. This allowed further to derive photometric redshifts for these sources, by employing the empirical ANNz algorithm (Collister & Lahav 2004) trained on subsamples drawn from spectroscopic redshift surveys overlapping with 2MASS. The 2MPZ is an extension of earlier attempts by Jarrett (2004) and Francis & Peacock (2010) who derived less accurate photo-z's for 2MASS, not having access to the WISE data collected in 2010. The median redshift of the 2MPZ sample is $\bar{z} = 0.08$ and its typical photo-z errors are 13% (RMS in δz of ~ 0.013).

3.2 Sample selection

Even though 2MASS has virtually 100% sky coverage, a number of observational effects will inevitably reduce the fraction of the sky that can be used for cosmological studies. The most important of these result from our Galaxy obscuring the view and creating the so-called Zone of Avoidance. In addition, as 2MPZ was built by cross-correlating the 2MASS XSC with WISE and SuperCOSMOS, the two latter catalogues bring their own additional incompletenesses, which need to be accounted for. In order to determine the regions of the sky that should be masked for the subsequent analysis, we have performed a standard study of source number counts in the presence of the different possible systematics. For the 2MASS XSC, and hence 2MPZ, there exist 4 potential sources of systematic effects: Galactic dust extinction, stars, seeing and sky brightness. The effects of each of these on the angular correlation function of 2MASS galaxies were studied by Maller et al. (2005), who found that both sky brightness and seeing had a negligible effect. We have therefore focused our analysis on dust extinction and star density.

For a particular region in the sky, the contamination due to Galactic dust can be quantified in terms of the K-band correction for Galactic extinction, $A_K = 0.367\,E(B-V)$, where the reddening $E(B-V)$ was derived for the whole sky by Schlegel et al. (1998). Star density in turn was computed at the position of each 2MASS extended sources based on local counts of point sources (stars) brighter than $K_s = 14$ mag (Skrutskie et al. 2006). This information (log star density per deg^2) is provided for every source in the public 2MPZ database, and can be used to create a full-sky map of $n_{\rm star}$. We generated maps of A_K and $n_{\rm star}$ using the HEALPix[5] pixelization scheme (Górski et al. 2005) with a resolution parameter `Nside` $= 64$ (pixels of $\delta\Omega \simeq 0.84\,{\rm deg}^2$). This is the fiducial resolution that was used for most of this work, unless otherwise stated.

Following an analysis similar to Afshordi et al. (2004) we computed the angular number density of sources for objects with different magnitude K_s and residing in pixels with a different value of A_K and $n_{\rm star}$, and selected threshold

[3] This scaling factor has traditionally been labelled D instead of B, but we use a different convention here to avoid any confusion with the fractal dimension.

[4] Available for download from http://surveys.roe.ac.uk/ssa/TWOMPZ.

[5] http://healpix.sourceforge.net/

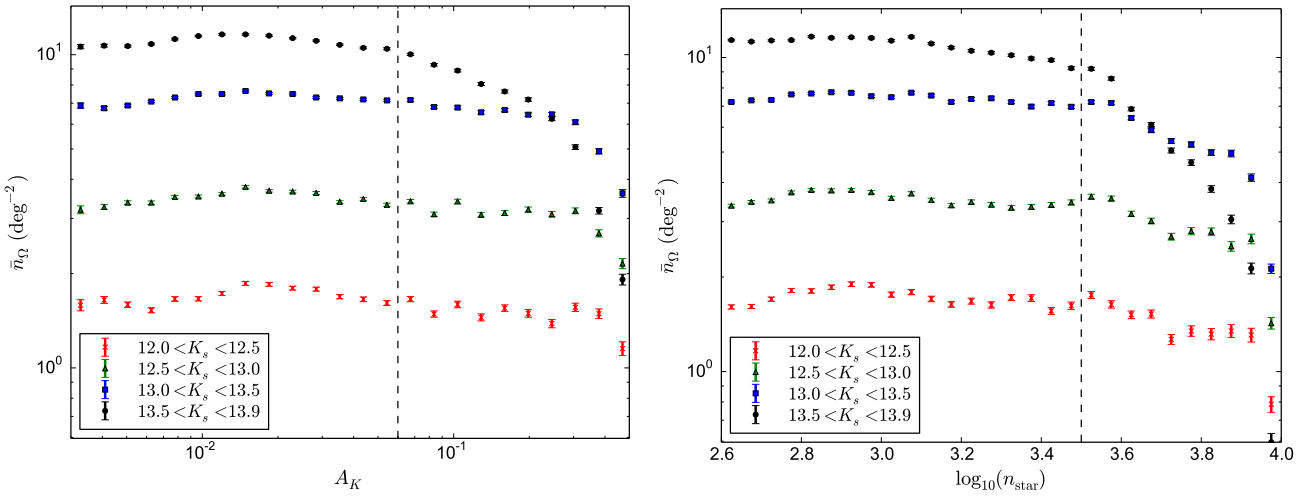

Figure 1. Number density of 2MPZ galaxies in 4 bins of magnitude measured in pixels with varying dust extinction (left panel) and star density (right panel). The vertical dashed lines show the values of $A_{K,\rm max}$ and $n_{\rm star,max}$ chosen to avoid these two systematics.

values $A_{K,\rm max}$ and $n_{\rm star,max}$ as those beyond which a substantial decrease in the observed number densities was observed. The results are shown in Figure 1 for dust extinction (upper panel) and star density (lower panel). In view of this result we chose the thresholds $A_{K,\rm max} = 0.06$ and $\log_{10}(n_{\rm star,max}) = 3.5$, which eliminates the areas near the Galactic plane and at the Magellanic Clouds (the latter were additionally cut out manually for better completeness), reducing the usable sky fraction to about 69%. Besides this, a small subset of pixels had to be discarded due to incompleteness in WISE and SuperCOSMOS. The former, in its 'All-Sky' release used for 2MPZ construction, is incomplete in two strips at Ecliptic $\lambda, \beta = 100°, +45°$ and $290°, -45°$ due to so-called "torque rod gashes"[6]; these were masked out manually. In the latter, a small fraction of data were missing due to issues with "stepwedges", which affected mostly plate corners; these create a regular pattern near the equator and were identified by comparison of the parent 2MASS XSC dataset with the final 2MPZ sample. The same comparison allowed us also to identify other sources of incompleteness brought about by WISE and SuperCOSMOS, which is mostly saturation around the brightest stars. The final footprint used for the best part of our analysis is shown in Figure 2 together with the maps of A_K and $n_{\rm star}$, and covers $f_{\rm sky} = 0.647$.

For most of this work we used a fiducial sample of galaxies with $12.0 < K_s < 13.9$. The lower magnitude cut was chosen to slightly reduce the number of local structures that could complicate the analysis, as well as the interpretation of the results. The upper cut was in turn estimated by Bilicki et al. (2014) to give a uniform sky coverage. It is worth noting that we verified that slight variations in these magnitude limits did not vary our results significantly. Taking into account the mask described above, our fiducial sample contains 628280 galaxies. In the analysis of the homogeneity index (Section 4.2), we have further divided the survey into two photometric redshift bins, with $0.03 \leqslant z_{\rm ph} < 0.08$ and $0.08 \leqslant z_{\rm ph} \leqslant 0.3$, each containing 264158 and 351383 objects respectively. From here on we will refer to these subsamples as "Bin 1" and "Bin 2". The number density field corresponding to our fiducial sample is displayed in the upper panel of Figure B1.

In order to verify that the cuts defining our sample do not introduce any systematic biases in our results we have studied their effect on the 2-point clustering statistics as well as the presence of hemispherical asymmetries in our final density maps. This is described in Section 4.3.

3.3 Clustering analysis and galaxy bias

In order to characterize the possible deviations from statistical homogeneity that we will study in the next Section, it is necessary to compare them with the expected statistical uncertainties allowed within the standard cosmological model. The most reliable way of estimating these is by using mock galaxy catalogues that reproduce the statistical properties of our survey. For this we have used the method described in Appendix A, which requires a correct model of the best-fit angular power spectrum of the data.

A crucial step in characterizing the clustering statistics of our galaxy sample within ΛCDM is modelling its redshift distribution dN/dz. Although 2MPZ provides photometric redshifts for all the sources with a remarkably small uncertainty (on average), it is not possible to estimate the true dN/dz reliably using these: $dN/dz_{\rm phot}$ is a convolution of the underlying $dN/dz_{\rm spec}$ with the photometric redshift error, which typically makes the photo-z distribution narrower than the true one. Fortunately, at high Galactic latitudes $b \gtrsim 60°$ there is practically full spectroscopic coverage from SDSS[7], which we can use for this task[8]. In total we identified a subset of $\sim 10^5$ objects in this region with spectroscopic

[6] http://wise2.ipac.caltech.edu/docs/release/allsky/expsup/sec6_2.html#lowcoverage

[7] 2MPZ used SDSS Data Release 9 (Ahn et al. 2012).

[8] Spectroscopic redshifts, where available, are also provided in the 2MPZ database.

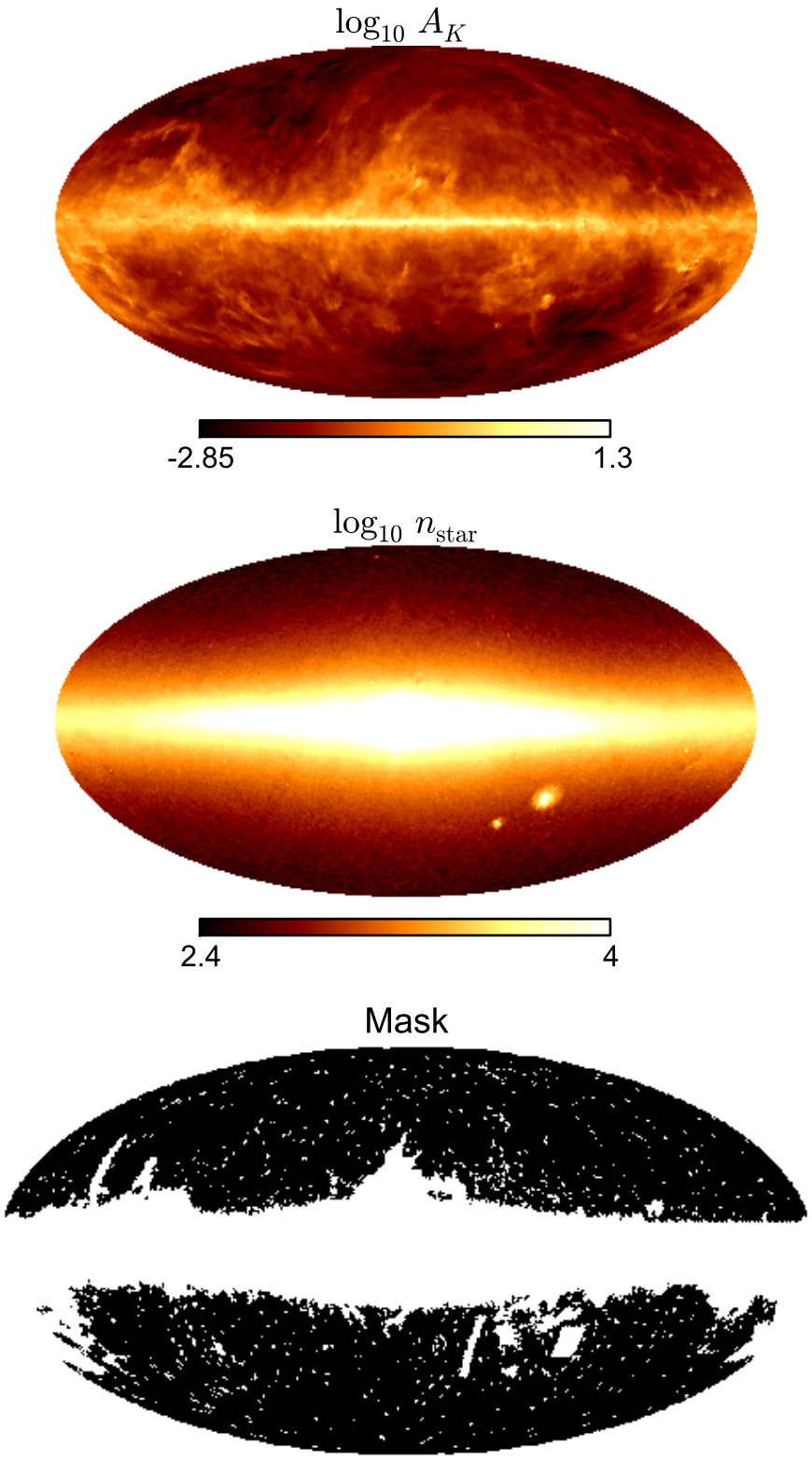

Figure 2. Sky maps of the two main sources of systematics: dust extinction (upper panel) and star density (middle panel). Our final mask is shown in the lower panel, and was defined by minimizing the effects of these systematics as described in Sections 3.2 and 4.3.

Sample name	Cuts	$N_{\rm gal}$	α	β	z_0	Bias b
Fiducial	$K_s \in [12, 13.9]$	628280	2.21	1.43	0.053	1.24 ± 0.03
Bin 1	$K_s \in [12, 13.9]$ & $z_{\rm ph} \in [0.03, 0.08)$	264158	2.61	3.36	0.066	1.18 ± 0.03
Bin 2	$K_s \in [12, 13.9]$ & $z_{\rm ph} \in [0.08, 0.3]$	351383	6.51	1.30	0.032	1.52 ± 0.03

Table 1. Summary of the galaxy samples used in this work. Column 2 lists the cuts imposed in each case (besides those used to define the mask), and column 3 lists the total number of objects in each sample. Columns 4-6 contain the best-fit parameters for the redshift distributions according to the model in Eq. 17, and column 7 shows the value of the best-fit galaxy bias.

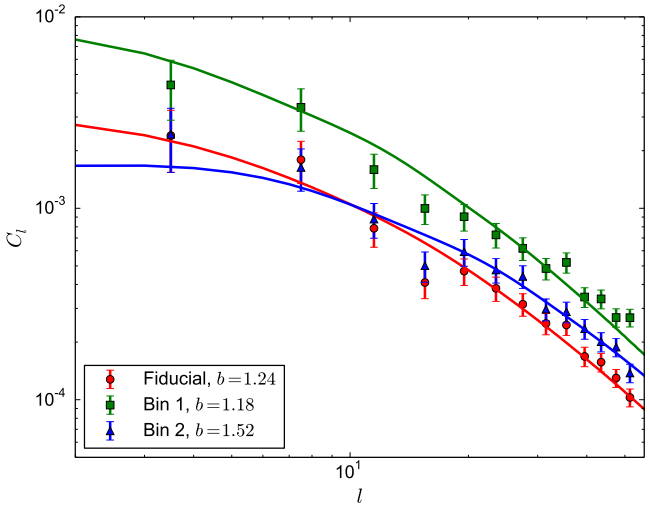

Figure 3. Angular power spectrum measured for the three samples listed in table 1 (points with error bars) together with the ΛCDM prediction (solid lines) using the best-fit bias parameters.

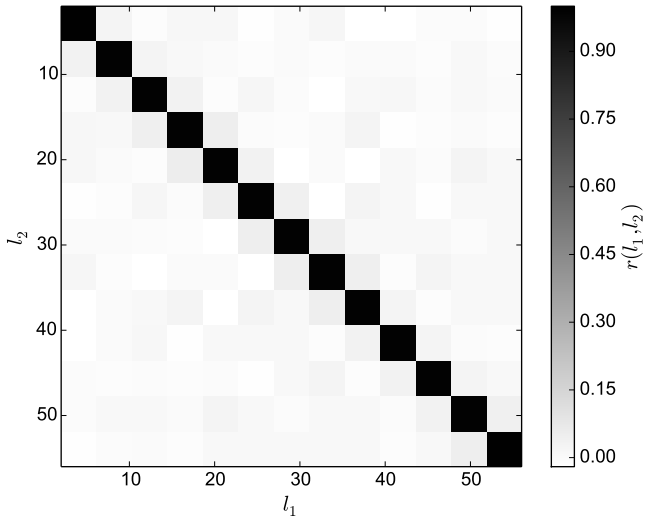

Figure 4. Correlation matrix ($r_{ij} \equiv \mathcal{C}_{ij}/\sqrt{\mathcal{C}_{ii}\mathcal{C}_{jj}}$) of the uncertainties in the angular power spectrum for our fiducial sample. The measurements in different bins of l are almost completely uncorrelated.

redshifts measured by SDSS, which we binned to estimate the redshift distributions of our galaxy samples. We fit a smooth function of the form

$$\frac{dN_{\rm model}}{dz} \propto z^{\alpha} \exp\left[-\left(\frac{z}{z_0}\right)^{\beta}\right] \qquad (17)$$

to each of these histograms, obtaining the best-fit parameters listed in Table 1. In order to verify that the redshift distribution estimated from this spectroscopic sample can be extrapolated to the rest of the survey, we calculated the angular two-point correlation function in this region and in the whole survey for our fiducial sample and compared both of them. A difference in the redshift distributions would cause a difference in the amplitude of the correlation functions, which we did not observe.

For each of the three subsamples listed above (Fiducial, Bin 1 and Bin 2) we determined a single effective bias parameter b that best fits its clustering statistics. To do this we first created a map of the projected overdensity of galaxies with the angular resolution parameter `Nside` $= 64$ by assigning to each pixel i the value $\delta_i = N_i/\bar{N} - 1$, where N_i is the number of galaxies in that pixel and $\bar{N}$ is the average number of galaxies per pixel. We then computed the angular power spectrum C_l of this overdensity field, fully accounting for the angular mask using the PolSpice software package (Chon et al. 2004). The theoretical power spectrum we fitted to these data was calculated using the fits to the redshift distribution described above as proxy for the radial window function ($W(\chi)\chi^2 d\chi/dz \propto dN/dz$) and Equations 2 and 3, with the linear power spectrum at $z = 0$, $P_0(k)$, predicted by CAMB (Lewis et al. 2000). We fixed all cosmological parameters except for the linear galaxy bias to their best-fit values as measured by Planck Collaboration et al. (2014a), $(\Omega_M, \Omega_\Lambda, \Omega_b, h, \sigma_8, n_s) = (0.315, 0.685, 0.049, 0.67, 0.834, 0.96)$. The best-fit value of the bias b was found by minimizing the χ^2:

$$\chi^2 \equiv \sum_{l_1,l_2} [\hat{C}_{l_1} - C^{\rm model}_{l_1}(b)]\, \mathcal{C}^{-1}_{l_1 l_2} [\hat{C}_{l_2} - C^{\rm model}_{l_2}(b)], \qquad (18)$$

where $\hat{C}_l$ is the measured power spectrum, $C_l(b)$ is the linear ΛCDM model for a bias b and $\mathcal{C}_{l_1 l_2}$ is the covariance between different multipoles.

For this exercise we assumed a diagonal covariance matrix, estimated theoretically as (Francis & Peacock 2010; Crocce et al. 2011):

$$\mathcal{C}_{l_1 l_2} = \frac{2}{f_{\rm sky}(2l_1+1)} \left(\hat{C}_{l_1} + \frac{1}{\bar{n}_\Omega}\right) \delta_{l_1 l_2}. \qquad (19)$$

This assumption is exact for a statistically isotropic distribution observed across the whole sky, however it is well known that partial sky coverage introduces correlations between different multipoles. In order to avoid this we grouped the multipoles into bins of width $\Delta l = 4$, thus reducing the correlation between neighbouring bins. A posteriori we also confirmed the validity of this approximation by computing the full covariance matrix $\mathcal{C}_{l_1 l_2}$ from 10000 mock catalogues generated using our best-fit values for the bias b (see Figure 4) . It is also worth noting that in order to avoid using an

incorrect model for the angular power spectrum or its covariance matrix due to small-scale non-linearities we limited the range of multipoles used for this analysis to $l \in [2, 56]$, corresponding to scales $k \lesssim 0.3\,h\mathrm{Mpc}^{-1}$.

The best-fit values of b in the three samples are listed in the last column of Table 1, and are in good agreement with prior estimates of the bias for 2MASS galaxies (Maller et al. 2003; Frith et al. 2005; Francis & Peacock 2010). Figure 3 shows the power spectra computed in our three samples together with their best-fit theoretical predictions. It is worth noting that these estimates rely heavily on the assumed amplitude of the dark matter power spectrum (i.e. σ_8), and therefore our results must be understood as measurements of the combination $b \times (\sigma_{8,\mathrm{Planck}}/\sigma_8)$, with $\sigma_{8,\mathrm{Planck}} = 0.834$.

4 RESULTS

This Section presents in detail our analysis regarding the fractality of the galaxy distribution in our sample. Sections 4.1 and 4.2 discuss respectively the scaling relations and the angular homogeneity index derived for the 2MPZ sample, while in Section 4.3 we analyse the possible systematic effects that could have an impact on these results, including the presence of significant hemispherical or dipolar asymmetries.

4.1 Scaling relations

As a means to probe the possible fractal structure of the galaxy distribution we have studied the scaling of the number density and angular correlation function of galaxies with magnitude limit and verified the predictions described in Section 2.3 for homogeneous cosmologies.

In order to form a quantitative idea regarding the agreement of our results with the standard cosmological model we have compared the results obtained from the 2MPZ catalogue with those of a suite of mock realizations of the fractal β-model, described in Appendix B. These mocks were made to follow the K_s-band luminosity function estimated by Appleby & Shafieloo (2014), and span a physical volume equivalent to that probed by 2MPZ. Note that the luminosity function used to simulate the fractal realizations was derived from the 2MPZ data assuming a FRW background, and it is therefore inconsistent in principle to apply it to the inhomogeneous fractal models. However, since we only aim to use the scaling relations as a consistency test of the CP, the use of this luminosity function does not affect our final results. We generated 100 mock realizations for 3 different values of the fractal dimension: $D = 2.5$, 2.75 and 2.90.

4.1.1 Number density

As shown in Section 2.3, for a homogeneous Universe the number of galaxies observed by a survey with magnitude limit m_{lim} should follow an exponential distribution given by equation 15. Consequently the probability distribution function of magnitudes should follow a similar behaviour with the same index $\beta = 0.6$:

$$\log_{10} \mathrm{pdf}(m) = \beta\, m + C. \qquad (20)$$

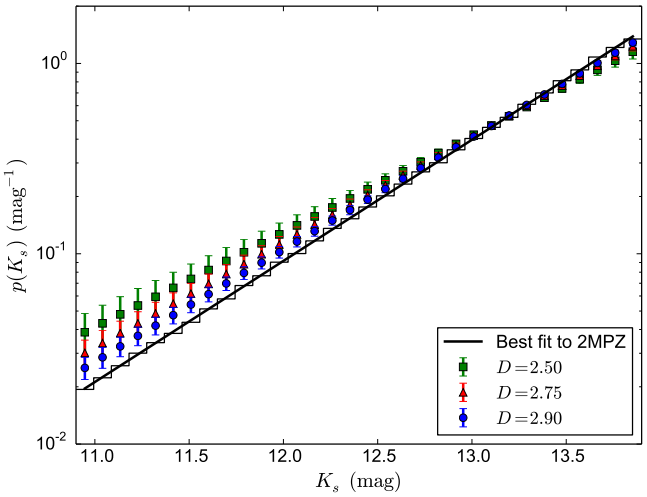

Figure 5. Probability distribution for K_s derived from the number counts histograms for fractal models with different fractal dimensions (points with error bars) together with the best-fit parametrization $\beta = 0.63$ for the 2MPZ sample (black solid line). The black histogram shows the actual 2MPZ data.

Deviations with respect to $\beta = 0.6$ can be expected within the standard model due to clustering variance and shot noise, and the exact uncertainty on this parameter is difficult to assess without an accurate model of the three-dimensional distribution of galaxies.

In order to estimate β from the data we made a histogram of the number counts of galaxies as a function of apparent magnitude in the K_s band. The value of β was computed by fitting the logarithmic number counts to the linear model in Eq. (20). Doing this we obtained a best-fit value $\beta = 0.63$, which is 5% above the homogeneous value. Understanding the significance of this deviation requires computing the uncertainty on this parameter, which is related to the variance of the number counts. As we discuss further in the context of hemispherical asymmetries (Section 4.3.2), the errors in the number counts are dominated by cosmic variance, and are a factor of ~ 12.5 larger than the Poisson errors ($\propto \sqrt{N}$) for our fiducial sample. In order to estimate the error of β we have therefore used the Poisson error of the histogram scaled by a constant factor of 12.5, obtaining $\Delta\beta \simeq 0.015$, i.e. our measurement is consistent with the homogeneous prediction within $\sim 2\sigma$. Similar positive deviations have also been reported by other studies (Sandage et al. 1972; Afshordi et al. 2004). As noted by Keenan et al. (2010), a positive deviation with respect to the homogeneous $\beta = 0.6$ value also suggests that the local Universe could be under-dense on scales of a few hundred Mpc. This underdensity could have an impact in explaining the differences between local measurements of the expansion rate and those derived from CMB observations (Keenan et al. 2012).

The values of β measured from the mock fractal realizations further support this result. Figure 5 shows the mean value and standard deviation of the normalized number-counts histograms for the three different values of the fractal dimension $D = 2.5$, 2.75 and 2.9, together with the best-fit

prediction for the 2MPZ data. The measured values of β are

$$\beta(D = 2.50) = 0.51 \pm 0.05,$$
$$\beta(D = 2.75) = 0.55 \pm 0.03,$$
$$\beta(D = 2.90) = 0.59 \pm 0.02,$$

in excellent agreement with the prediction $\beta = 0.2\,D$. We can see that the value measured from the data lies more than 2 standard deviations away from the fractal predictions for $D = 2.5$ and 2.75.

4.1.2 Scaling of the angular 2-point correlation function

In order to test the scaling law for the angular correlation function as a function of magnitude limit, Eq. (16), from the 2MPZ sample, we generated four subsamples with different maximum K_s magnitude. These were chosen to have the same bright limit $K_{s,\rm min} = 12.0$ and a varying faint limit $K_{s,\rm max} = 12.5$, 13.0, 13.5 and 13.9.

For each of these subsamples we compute the angular two-point correlation function using the estimator introduced by Landy & Szalay (1993):

$$w(\theta) = \frac{DD(\theta) - 2DR(\theta) + RR(\theta)}{RR(\theta)}, \qquad (21)$$

where DD, DR and RR are the normalized counts of pairs of objects separated by angle θ for "data-data", "data-random" and "random-random" pairs respectively. The correlation function was estimated using the software presented in Alonso (2012), with random catalogues containing 10 times as many objects as our data. In order to compute the statistical uncertainties in $w(\theta)$ we divided our catalogue into $N_{\rm S} = 50$ samples, each covering approximately the same area. These were chosen evenly in the north and south Galactic hemispheres in the region with $|b| > 13°$. The covariance matrix $C_{i,j} \equiv \langle \Delta w(\theta_i) \Delta w(\theta_j) \rangle$ was estimated as the sample covariance matrix of the measurements of $w(\theta)$ made in each of these samples scaled by a factor $1/N_{\rm S}$ to account for the smaller area covered by each of them:

$$\hat{C}_{ij} = \sum_{n=1}^{N_{\rm S}} \frac{[w_n(\theta_i) - \bar{w}(\theta_i)][w_n(\theta_j) - \bar{w}(\theta_j)]}{N_{\rm S}(N_{\rm S} - 1)}, \qquad (22)$$

where w_n is the angular correlation function measured in the $n-$th region and $\bar{w} \equiv \sum_n w_n/N_{\rm S}$. The inverse covariance matrix used later to compute the χ^2 was estimated in terms of the inverse of $\hat{C}_{ij}$ as (Hartlap et al. 2007)

$$[\tilde{C}^{-1}]_{ij} = \frac{N_S - n_\theta - 2}{N_S - 1} [\hat{C}^{-1}]_{ij}, \qquad (23)$$

where n_θ is the number of bins of θ in which the correlation function was measured.

As is now well known in the field (Maller et al. 2005; Crocce et al. 2011), the measurements of the angular correlation function show large correlations between different angles, and therefore it is important to consider the non-diagonal elements of the covariance matrix in order to assess the goodness of fit of a particular model. These large off-diagonal elements strongly penalize any deviation from the theoretical model and can cause a seemingly valid model to yield a bad minimum χ^2. Furthermore, these correlations often cause the covariance matrix to be almost degenerate and difficult to invert due to statistical noise. Since the number of independent realizations needed to estimate an invertible $n_\theta \times n_\theta$ covariance matrix is usually of the order n_θ^2, we performed the fits described below in a reduced range of scales (clearly stated in each case).

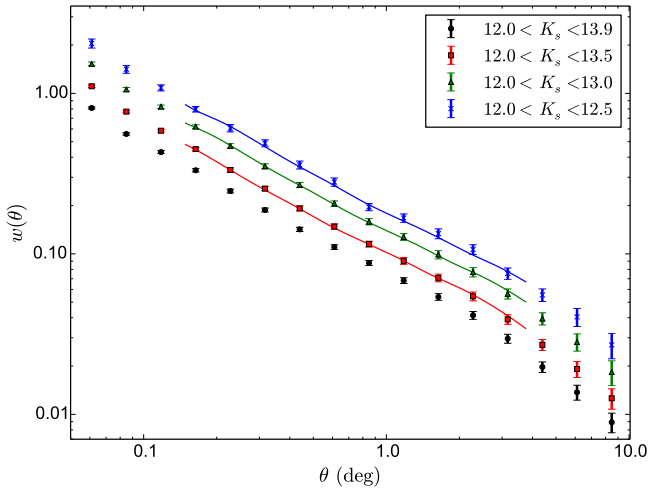

Figure 6. Angular correlation functions for the four K_s-magnitude bins considered in this analysis. The points with error bars show the actual measurements and estimated uncertainties, while the solid lines correspond to the best fit templates rescaled using Equation 24.

$(K_{s,\rm min}, K_{s,\rm max})$	B	χ^2/dof	p-value
(12.0,13.5)	0.85 ± 0.01	0.91	0.51
(12.0,13.0)	0.71 ± 0.01	0.72	0.70
(12.0,12.5)	0.61 ± 0.01	1.45	0.16

Table 2. Values of the scaling parameter B measured from the angular correlation function in different magnitude bins, together with their reduced χ^2 and associated p-value for the best-fit model in Eq. (24).

In order to test the scaling relation in Equation 16 we use the measured correlation function in the fiducial magnitude bin $12.0 < K_s < 13.9$ as a template that we can rescale to fit for the scaling parameter B in the other bins. Other possibilities would be using a template based on the theoretical prediction for the correlation function or a simple power-law model. The latter option has been shown to be a bad approximation to the correlation function on small-scales (Maller et al. 2005), while the former is affected by theoretical uncertainties. Since our method uses only observed quantities, we avoid any of these potential biases, and purely test the predicted scaling relation. Our method is therefore:

(i) We find the cubic spline $W_{\rm sp}(\theta)$ that interpolates through the measurements of the correlation function in our widest magnitude bin.

(ii) We use a rescaling of this spline as a template to fit for the scaling parameter B in the other three bins. Thus, for each bin we find the parameter B that best fits the data given the model

$$w(\theta, B) = \frac{W_{\rm sp}(B\theta)}{B}. \qquad (24)$$

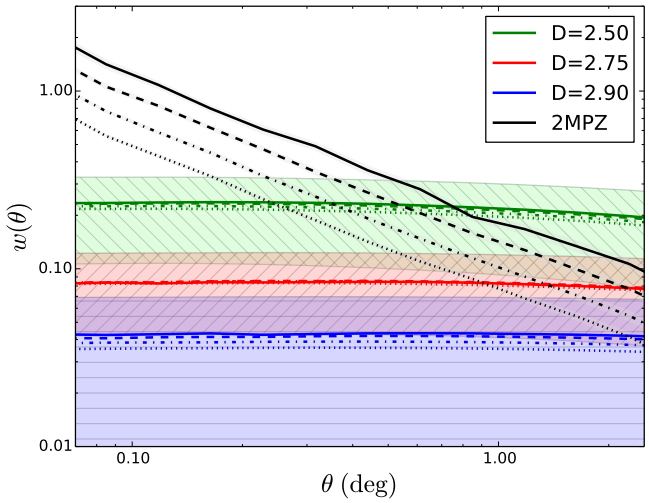

Figure 7. Mean (lines) and variance (coloured bands) of the angular correlation function in a suite of 100 mock fractal realizations described in Appendix B. The results for fractal dimensions $D = 2.5$, 2.75 and 2.9 are shown in green, red and blue respectively, while the correlation functions measured from 2MPZ are shown as black lines. In all cases solid, dashed, dot-dashed and dotted lines correspond to the mean correlation function in the magnitude bins $K_s \in (12.0, 12.5)$, $K_s \in (12.0, 13.0)$, $K_s \in (12.0, 13.5)$ and $K_s \in (12.0, 13.9)$ respectively, and the coloured bands around them show the 1σ deviations. Fractal models show a much milder variation in the amplitude of $w(\theta)$ as a function of magnitude limit.

This fit is performed by minimizing the corresponding χ^2 using the full covariance matrix.

In order to avoid using an incorrect template due to the statistical uncertainties in the correlation function of the first magnitude bin, caused by shot noise (mainly on the smallest scales) and cosmic variance (largest scales), we performed this fit in the range $0^\circ.16 < \theta < 3^\circ.15$, using 10 logarithmic bins of θ.

The values of B estimated using this method are shown in Table 2 together with their corresponding χ^2. These results are also displayed in Figure 6. In all cases we find that the scaling law is a good description of the relation between the correlation functions with different magnitude limits. The agreement between the measured values of B and the prediction $B \sim \sqrt{F_1/F_2}$ is difficult to address due to the presence of a low magnitude cut. However, in the case of the first magnitude bin ($B = 0.85 \pm 0.01$), which is less affected by this cut, the agreement is excellent ($\sqrt{F_1/F_2} \simeq 0.83$). For the narrowest bin ($12.0 < K_s < 12.5$) we find a slightly higher χ^2/d.o.f., which is still statistically insignificant well within 2σ.

As described in Section 2.3, larger structures are found in a perfect fractal model as the survey depth is increased, and thus the amplitude of the angular correlation function should stay almost constant with the magnitude limit. We have tested this explicitly using the mock fractal realizations described in Appendix B. We computed the angular correlation functions, in the same magnitude bins, from a suite of 100 mock catalogues with fractal dimensions $D = 2.5$, 2.75 and 2.9. The coloured lines in Figure 7 show the mean correlation functions measured for 12 different cases: $D = 2.5$ in green, $D = 2.75$ in red and $D = 2.9$ in blue, with different line styles showing the results for the different magnitude bins (see description in caption). The coloured bands around these lines show the 1σ dispersion around this mean estimated from the 100 realizations. For comparison, the correlation functions measured in 2MPZ are also shown as black lines in this plot. Although the variance associated with fractal models is significantly larger than in the standard cosmological model, it is easy to see that the amplitude of the correlation function varies a lot less with the magnitude limit in these models. While this amplitude roughly doubles in the 2MPZ data from the deepest to the shallowest magnitude bin, we do not observe variations larger than $\sim 10\%$ between the mean correlation functions of the fractal realizations. Although this is further evidence of the compatibility of our our measurements with the standard cosmological model, the large variance of the correlation function in fractal scenarios makes it difficult to impose tighter constraints on them.

4.2 The angular homogeneity index

We have studied the possible fractal nature of the galaxy distribution in the 2MPZ sample further by analysing the angular homogeneity index $H_2(\theta)$, described in Section 2.2. In order to optimize the use of our data, we have used the estimator **E3** described in Alonso et al. (2014), to measure this quantity. This estimator is based on the method used by Scrimgeour et al. (2012) to measure the fractal dimension, and makes use of a random catalogue with the same angular mask as the data to correct for edge effects. The process is as follows:

(i) For the i-th object in the data, we compute $n_i^d(<\theta)$ and $n_i^r(<\theta)$, the number of data and random objects respectively found in a spherical cap of radius θ centered on i.

(ii) For N_c objects in the data thus used as centres of spherical caps, we define the scaled counts-in-caps $\mathcal{N}(\theta)$ as

$$\mathcal{N}(\theta) = \frac{1}{N_c}\sum_{i=1}^{N_c}\frac{n_i^d(<\theta)}{f_r\, n_i^r(<\theta)}, \qquad (25)$$

where $f_r \equiv D/R$ is the ratio between the number of data and random objects.

(iii) $\mathcal{N}(\theta)$ is directly related to the angular correlation integral $G_2(\theta)$ as

$$G_2(\theta) = \bar{N}(\theta)\,\mathcal{N}(\theta) - 1, \qquad (26)$$

where $\bar{N}(\theta)$ is the expected number of galaxies in a spherical cap of radius θ, $\bar{N}(\theta) \equiv \bar{n}_\Omega V(\theta) \equiv \bar{n}_\Omega\, 2\pi(1-\cos\theta)$, and we have explicitly subtracted the Poisson contribution due to linear shot-noise.

(iv) The homogeneity index is then estimated by numerical differentiation of G_2:

$$H_2(\theta) = \frac{d\log G_2(\theta)}{d\log V(\theta)}. \qquad (27)$$

The main advantage of this estimator is that, since it attempts to correct for edge-effects using random realizations, it is possible, in principle, to use all the objects in the data as centres for spherical caps of any scale θ, thus minimizing the statistical uncertainties on H_2. However, by doing

this we can potentially bias our estimate of $H_2(\theta)$ towards the homogeneous value $H_2 = 1$. The reason for this is that weighting by the random number counts n_i^r is equivalent to assuming that our sample is homogeneous in the parts of the spherical caps that lie inside the masked regions. Therefore this potential bias will be more important for larger θ, for which a larger fraction of the spherical caps will be masked. In order to limit the effects of this bias we have performed two different tests:

- Using the mask described in Section 3.2 (see bottom panel in Figure 2) we found, for every unmasked pixel, all other pixels lying within a distance θ from it and computed the fraction of those pixels that are unmasked. We thus estimated the average completeness of spherical caps as a function of their radius θ. The potential systematic edge effects mentioned in the previous paragraph should become more important as this completeness decreases, and thus we can limit their impact by constraining our analysis to scales with a mean completeness above a given threshold. We determined that using a fiducial completeness threshold of $> 75\%$ limits the spherical caps that can be used for our analysis to scales smaller than $\theta_{\rm max} = 40^\circ$. A more stringent completeness cut of 85% would translate into a scale cut $\theta \lesssim 20^\circ$.
- For scales below the threshold $\theta_{\rm max}$ it would be desirable to estimate the magnitude of the systematic error induced on the measurement of $H_2(\theta)$ by the incomplete sky coverage. This can be done using the fact that these systematic effects should vanish entirely in the absence of an angular mask, and thus they can be quantified by comparing the measurements made on simulated catalogues with and without mask. We computed the mean value of $H_2(\theta)$ in our fractal and lognormal realizations in these two cases and estimated the average fractional deviations between them. For our lognormal realizations, as well as for the fractal mocks with $D = 2.9$ and $D = 2.75$, a small systematic bias smaller than $0.1 - 0.2\%$ is found, which increases to $\sim 0.6\%$ for $D = 2.5$. As we will see below, this small bias does not affect any of the results found in this work, and can therefore be neglected.

In view of these results we determined that limiting our analysis to scales $\theta < 40^\circ$ should limit the potential bias of our estimator to an acceptable level.

We computed the homogeneity index for our fiducial sample, as well as for the two photometric redshift bins listed in Table 1, in order to study the evolution of $H_2(\theta)$ with redshift. This was done in the range $\theta \in [0^\circ, 40^\circ]$, using 40 bins of width $\Delta\theta = 1^\circ$. The results are shown in Figure 8. In descending order each panel presents the results for our Fiducial sample, Bin 1 and Bin 2. The solid lines show our measurements from the 2MPZ catalogue, while the darker bands around them provide the 1σ uncertainties, estimated as the standard deviation of a suite of 200 lognormal mock catalogues (see Appendix A). The mean value of the mock realizations, shown as thin dashed lines in this figure, can be used as a proxy for the theoretical expectation within ΛCDM. As could be expected, due to the growth of structure and to projection effects (the same angular separation corresponds to shorter physical distances on small redshifts), the low-redshift sample (Bin 1) is more inhomogeneous than the high-redshift one. It is also worth noting that the measurements agree qualitatively well with the mean value of the lognormal realizations. This was not guaranteed a priori: even though lognormal realizations are able to reproduce the 2-point statistics of the galaxy distribution superbly, the homogeneity index depends also on higher-order correlations (Bagla et al. 2007).

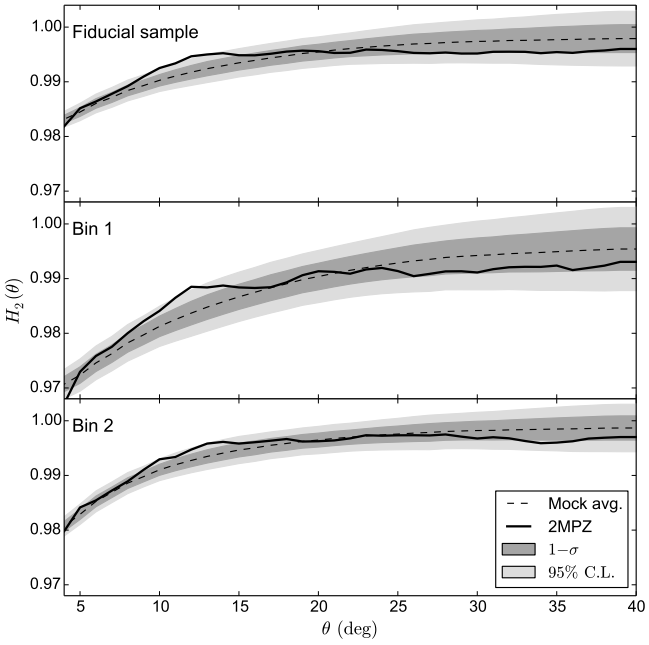

Figure 8. Angular homogeneity index computed in our three samples (see Table 1). In each panel the solid line shows our measurements from the 2MPZ data, while the dashed, thiner lines correspond to the mean value found for a suite of 200 lognormal mock catalogues. These mock realizations were used to compute the 1σ and 1.96σ (95% C.L) regions, shown as the darker and lighter bands around the measurements.

Sample name	θ_H (2MPZ)	θ_H (Mocks)	$f_{\rm above}$
Fiducial	35°	$26^\circ \pm 5^\circ$	10.5%
Bin 1	39°	$28^\circ \pm 5^\circ$	14%
Bin 2	24°	$24^\circ \pm 5^\circ$	54.5%

Table 3. Angular homogeneity scale for our three samples. The second column shows the values of θ_H measured from the data, while the third column shows the mean value and variance estimated from the mock catalogues. The last column shows the fraction of mock realizations in which homogeneity is attained on scales larger than the value of θ_H measured in the data.

The homogeneity index, as measured in 2MPZ, seems to approach the perfect homogenous prediction $H_2 = 1$ on large scales, although it deviates slightly from it. As we have mentioned, these deviations are expected within ΛCDM, and we should therefore quantify their significance. In order to do so we have estimated the angular scale of homogeneity θ_H, proposed in Alonso et al. (2014) as the largest angle for which the measured value of H_2 deviates from the homogeneous value of 1 at 95% C.L. (i.e. $1 - H_2(\theta_H) = 1.96\,\sigma_{H_2}(\theta_H)$, where σ_{H_2} is the statistical error on H_2). We computed θ_H for the same three samples as well as for their corresponding 200 mock realizations in order to quantify the expected variance of this quantity. For each sample we estimated the

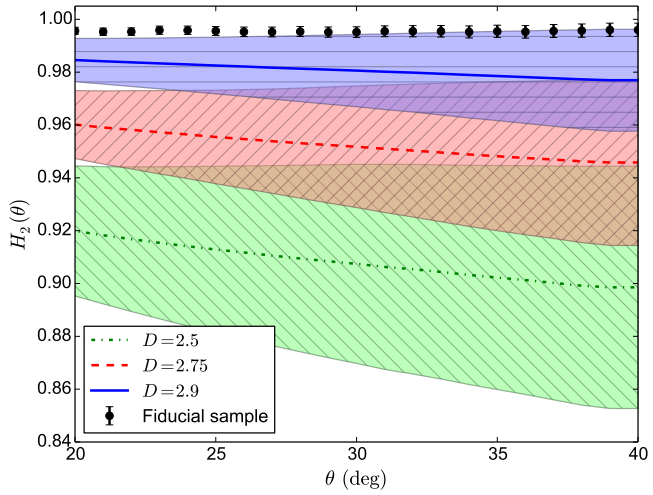

Figure 9. Angular homogeneity index measured from the 2MPZ data (points with error bars), as well as the mean value and variance (solid lines and light coloured bands respectively) estimated for the fractal β-model from the suite of mock catalogues described in Appendix B. The results for the fractal models correspond to fractal dimensions $D = 2.5$ (bottom curve, red), $D = 2.75$ (middle curve, green) and $D = 2.9$ (top curve, blue).

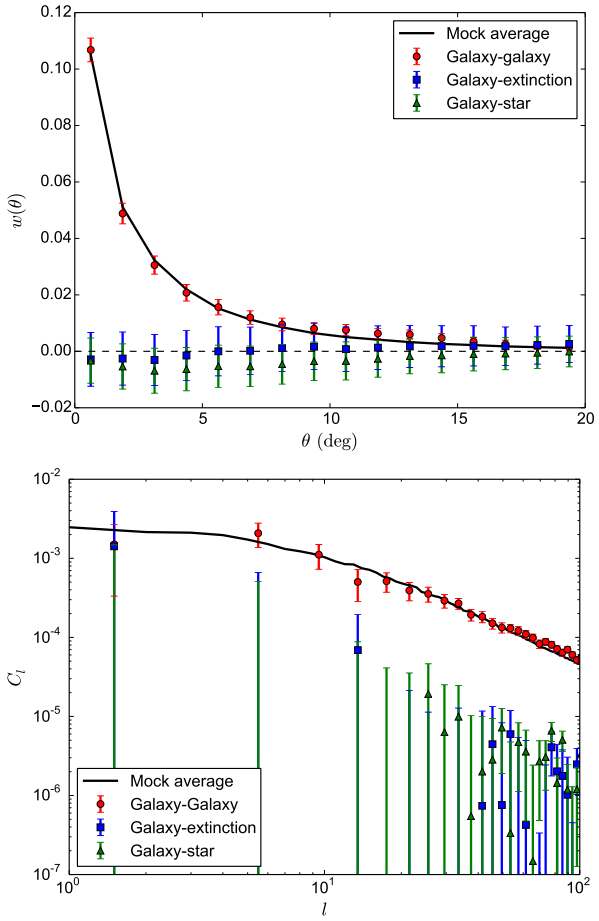

Figure 10. Auto- and cross- correlation in real space (top panel) and harmonic space (bottom panel) of the galaxy density field for our fiducial sample with the two potential sources of systematics: dust extinction (blue) and star density (green). The red points show the galaxy auto-correlation, which has a much bigger amplitude than any of the cross-correlations, both of which are consistent with 0. The correlations were computed for our fiducial mask, and the error bars were estimated using 100 mock catalogues described in Appendix A.

mean value of θ_H and its variance from the mock lognormal catalogues, as well as the fraction of mock catalogues in which homogeneity is reached on scales larger than the value of θ_H found in the 2MPZ data ($f_{\rm above}$). The results are summarized in Table 3: in agreement with our previous result, we find that our samples containing low-redshift objects ("Fiducial" and "Bin 1") reach homogeneity on scales exceeding the average value found in the mock realizations by about 2 standard deviations. The higher-z sample ("Bin 2"), nevertheless, agrees very well with the expected value of $\theta_H \simeq 24^\circ$. In all cases at least 10% of the mock realizations were found to reach homogeneity on scales larger than the values of θ_H measured in the data, which places the level of disagreement with the ΛCDM expectation well below 2σ.

Thus far we have shown that the measurements of $H_2(\theta)$ are fully compatible with the expectations of the standard cosmological model. However, we can also use these measurements of the asymptotic value of $H_2(\theta)$ to explore the viability of fractal models. As has been noted in the literature (Durrer et al. 1997), the fractal nature of a three-dimensional point distribution cannot be completely determined from its distribution projected on the sphere in a model-independent way, and therefore we cannot hope to rule out fractal models in general with this test. However, using the fractal β-model described in Appendix B we can study the values of $H_2(\theta)$ that can be expected from a cascading fractal model, which could potentially apply (at least qualitatively) to more general scenarios. Figure 9 shows the mean value and expected variance of $H_2(\theta)$ on large scales ($\theta > 20^\circ$) computed from a suite of 100 β-model realizations with fractal dimensions $D = 2.5$, 2.75 and 2.9, together with our measurements for the fiducial 2MPZ sample. The large-scale behaviour of the different projected distributions is clearly distinct, and allows us to quantify the disagreement between our measurements and these fractal models. We did so by computing the number of fractal realizations in which the value of $H_2(\theta)$ is consistently larger than our measurement from 2MPZ in the last 10 angular bins (i.e. $\theta > 30^\circ$), which we can interpret as the probability of finding a fractal Universe that is at least as isotropic as ours as implied by our measurements. While 12 of our 100 simulations with $D = 2.9$ are found above the measurements in our fiducial sample, this is not the case in any of the realizations with $D = 2.75$ or 2.5. This result reinforces the compatibility of our measurements with the standard cosmological model.

4.3 Systematics

In this Section we present a set of tests aimed at discarding possible systematic effects in our results which could arise from the sample selection described in Section 3.2.

4.3.1 Clustering systematics

In order to ensure that the cuts in dust extinction and star density specified in Section 3.2 are enough to prevent any significant systematic effect in the 2-point clustering statistics of the galaxy density field, we studied its cross-correlation with these two possible systematics.

We first generated maps of the anisotropies in the 2MPZ galaxy density, A_K and $n_{\rm star}$. This was done by computing, for each observable x and in each pixel i, the quantity $\delta_x^i = (x^i - \bar{x})/\bar{x}$, where $\bar{x}$ is the mean value of x averaged over all unmasked pixels. We then computed the cross- and auto-correlations of each pair of observables, $w_{x,y}(\theta) = \langle \delta_x \delta_y \rangle$, where the expectation value was estimated by averaging over all pairs of unmasked pixels subtending an angle θ. Figure 10 shows these cross correlations for our fiducial sample (see Section 3.3). The errors on these measurements were computed as the standard deviation for a suite of 100 mock galaxy catalogues described in Appendix A. In both cases the cross correlation of the galaxy overdensity with each systematic is compatible with 0, thus confirming our choice of $A_{K,\rm max}$ and $n_{\rm star,max}$. The bottom panel of Figure 10 shows the same auto- and cross- correlations in harmonic space (i.e. the power spectrum C_l), which confirm this result. Since, as stated above, the main contribution to the homogeneity index H_2 is due to the two-point correlation function, we do not expect any significant systematic effect on this quantity either.

4.3.2 Hemispherical differences

Assuming an isotropic galaxy distribution, an incorrect choice of A_K or $n_{\rm star,max}$ could cause an asymmetry in the properties of the galaxy sample in the north and south Galactic hemispheres. Likewise, errors in the calibration of the two twin facilities used to compile 2MASS, located in the two terrestrial hemispheres, could potentially generate a similar asymmetry with respect to the equatorial plane. Thus, investigating the presence of hemispherical differences is a good way of identifying systematic effects in a full-sky galaxy survey. Furthermore, this type of effects have been studied in different cosmological observations. Probably the most notable of these is the CMB dipolar asymmetry detected at $\sim 3.5\sigma$ in both Planck and WMAP (Park 2004; Eriksen et al. 2007; Hoftuft et al. 2009; Planck Collaboration et al. 2014b; Akrami et al. 2014) (although see (Quartin & Notari 2015)). Similar studies have been conducted with other datasets, including 2MASS (Gibelyou & Huterer 2012; Appleby & Shafieloo 2014; Yoon et al. 2014), radio galaxies (Fernández-Cobos et al. 2014), luminous red galaxies (Pullen & Hirata 2010), radio sources (Fernández-Cobos et al. 2014) and high-redshift quasars (Hirata 2009), finding however only marginal dipolar signals, if any. Understanding the origin of these asymmetries, when they arise, can not only shed light on the possible systematic effect affecting CMB measurements, but also tell us something about our relative motion with respect to the CMB rest frame (Itoh et al. 2010; Bilicki et al. 2011). Therefore, investigating the presence of these asymmetries in different datasets is also interesting in its own right, besides it being an additional test of the isotropy of the galaxy distribution.

We have searched for hemispherical differences both in the overall galaxy number counts and in the clustering variance of the galaxy overdensity.

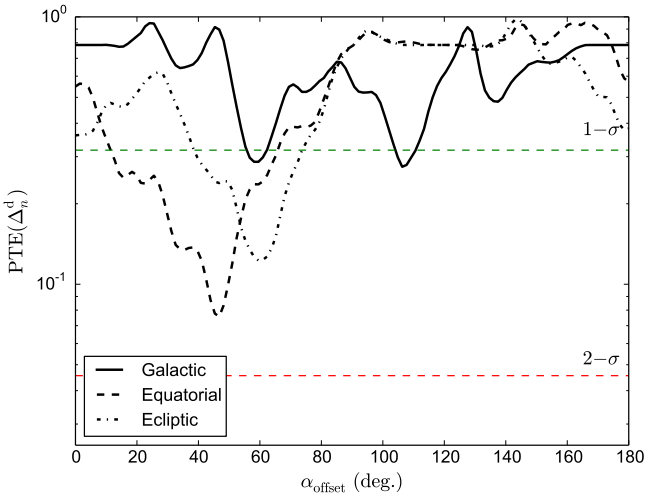

Figure 11. Probability to exceed for the normalized difference in the galaxy number counts measured in hemispheres defined by an angle α with respect to the three fundamental planes: Galactic (solid line), equatorial (dashed line) and ecliptic (dash-dotted line). In all cases the observed asymmetry can be explained by the statistical uncertainties for a ΛCDM model well within 2σ.

Number counts. We have studied the differences in the number of galaxies observed in two opposite hemispheres in our fiducial dataset ($12 < K < 13.9$) in relation to the variance of this difference expected within the standard cosmological model. In order to do so we considered hemispheres defined in terms of planes tilted by an angle α with respect to three fundamental planes: Galactic, ecliptic and equatorial. The reason for considering a varying angle α is that any potential systematic effects (for example, instrumental differences in the case of the equatorial plane) would become gradually more evident as $\alpha \to 0$. For each pair of hemispheres we computed the angular number density of galaxies in each of them as $\bar{n}_\Omega = N_{\rm gal}/(4\pi\, f_{\rm sky})$, where $N_{\rm gal}$ is the number of galaxies observed in that hemisphere and $f_{\rm sky}$ is the corresponding observed sky fraction (note that due to the incomplete sky coverage, $f_{\rm sky}$ will be different for both hemispheres and also for different values of α). In terms of these measurements, as a statistical observable we used the relative difference between both number densities:

$$\Delta_n \equiv \frac{2\,|\bar{n}_\Omega^N - \bar{n}_\Omega^S|}{\bar{n}_\Omega^N + \bar{n}_\Omega^S}. \tag{28}$$

We computed the value of Δ_n in the data as well as in 1000 independent mock catalogues, and used the mock measurements to estimate the probability distribution of this observable $p(\Delta_n|\alpha)$. We then characterized the compatibility between the number densities in each hemisphere measured in the data by computing the fraction of mocks for which we find a value of Δ_n larger than the one measured in the data, Δ_n^d:

$$\mathrm{PTE}(\Delta_n^{\rm d}, \alpha) \equiv \int_{\Delta_n^{\rm d}}^{\infty} p(\Delta_n|\alpha)\, d\Delta_n. \tag{29}$$

We note that, even for the fairly large volume probed by

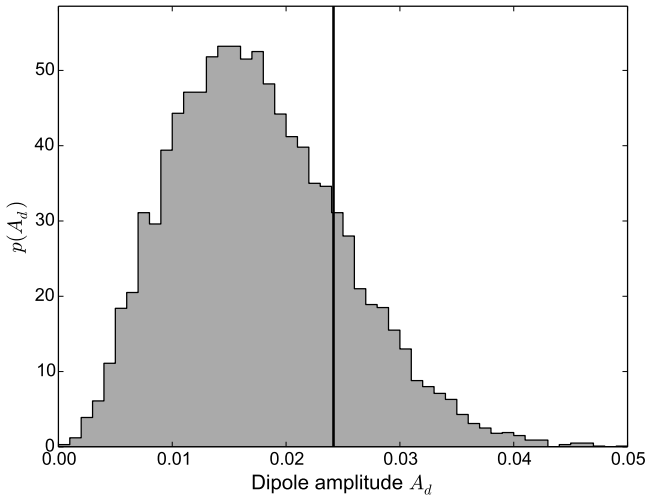

Figure 12. Probability distribution for the amplitude of the dipole in the local variance maps for disks of size 10°, derived from a suite of 10000 lognormal mock realizations. The value of A_d measured in our fiducial sample is shown as a vertical solid line in this Figure, and is in good agreement (within 1.3σ) with the expected ΛCDM value.

2MASS ($\chi(z_{\rm max}) \sim 800\,{\rm Mpc}/h$), the variance of Δ_n is by far dominated by clustering variance, and not Poisson noise. In comparison with the total error (cosmic variance + Poisson), computed from our lognormal realizations, Poisson errors are a factor of 12-13 times smaller. This must be taken into account when interpreting the significance of the observed asymmetries. The values of PTE(Δ_n^d, α) estimated through this method are shown in Figure 11 for the three fundamental planes. In no case do we find evidence for a hemispherical asymmetry in the galaxy number counts with a significance larger than 2σ.

Clustering. In order to detect possible hemispherical power asymmetries in our data we have performed an analysis similar to that carried out recently by Akrami et al. (2014) on CMB data. The method proceeds as follows:

(i) We first find disks of different angular sizes centered on the pixels of a HEALPix map of resolution `Nside` = 16 (i.e. 3072 pixels). For this analysis we considered disks of radius $\theta = 10^\circ$ and $\theta = 20^\circ$.

(ii) We create a map of the overdensity field for our fiducial sample as described in Section 3.3 using our fiducial pixel resolution `Nside` = 64. From this map we compute the variance of the overdensity field inside each of the disks found in the previous step. This yields a low-resolution map of the local variance. We neglect any disks for which more than 90% of the pixels were masked.

(iii) We repeat the previous step on a suite of 10000 mock lognormal realizations. From these we compute the mean local variance across the sky, as well as its standard deviation.

(iv) We subtract this mean map from the local variance map computed for our data, and fit a dipole to the resulting zero-mean map using an inverse-variance scheme. We perform the same operation on the local variance maps found for the 10000 mocks and store the values of the dipole amplitude A_d found in each case.

Disk radius	A_d	(l, b)	$p-$value
10°	0.024	(311°, 0°)	0.19 (1.3σ)
20°	0.028	(320°, 6°)	0.13 (1.5σ)

Table 4. Values dipole amplitude and direction in the local variance maps constructed for our fiducial sample, for disks of aperture 10° and 20°. The fourth column shows the fraction of mock catalogues found with a dipole amplitude A_d larger than the one measured in the data. In both cases the data is found to be compatible with the expected ΛCDM dipole well within 2σ.

(v) We characterize the significance of the power asymmetry in our data in terms of the number of mocks found with a value of A_d larger than the one found in our sample.

Figure 12 shows the distribution of dipole amplitudes A_d computed from the 10000 mock catalogues, for disks of size 10°, together with the value found in the data. The quantitative results are displayed in Table 4. For disks of both 10° and 20° we consistently found a dipole of amplitude $A_d \sim 0.025$ in the direction $(l, b) \sim (310^\circ, 5^\circ)$, which is close to the direction of the dipole found by Gibelyou & Huterer (2012) using 2MASS. The amplitude of this dipole is, however, in excellent agreement (within $\sim 1.5\sigma$) with the variance expected within ΛCDM. We can thus conclude that there are no significant hemispherical asymmetries in our data.

5 DISCUSSION

In this paper we have presented an analysis of the homogeneity and isotropy of the low-redshift galaxy distribution using data from 2MPZ. Making use of a set of observational probes relying mainly on angular information we have been able to study possible deviations of a fractal nature from the standard cosmological model. These probes included the scaling laws of the source number counts and angular correlation function as a function of magnitude limit and the measurement of the so-called homogeneity scale, which can be interpreted as the effective correlation dimension of the projected distribution. The 2MPZ sample is particularly well suited for this kind of studies for several reasons: first of all, its almost complete sky coverage makes it possible to study clustering on the largest angular scales. Secondly, the low median redshift of the survey implies that we can probe the evolution of the galaxy distribution at late times, where deviations from statistical homogeneity and isotropy due to gravitational clustering are potentially larger. Finally, the availability of photometric redshifts for all 2MPZ sources makes it possible to explore the evolution of the homogeneity index with redshift and compare that evolution with the expected behaviour within the ΛCDM model. We have found that, in terms of these observables, the data is in excellent agreement with the standard cosmological model, and no significant departure from its predictions has been observed.

The main results of this paper can be summarized as follows:

- Our measurements of the homogeneity index $H_2(\theta)$ show a good agreement of the data with the standard cosmological model, and we have verified that the galaxy distribution approaches homogeneity within the expected range

of angular scales. We have shown that this agreement holds also as a function of cosmic time by repeating the analysis in two bins of photometric redshift. We repeated this analysis on a suite of mock fractal realizations and found that none of those with fractal dimensions $D \lesssim 2.75$ approached homogeneity faster than the 2MPZ sample.

- We have shown that the measurements of the scaling laws for number counts and correlation function closely follow the expectation of a statistically homogeneous cosmology, while our tests using a particular fractal scenario (see Appendix B) have shown that these models display evident tension with these observables for fractal dimensions $D \lesssim 2.75$.
- As part of our search for systematics we perform an extra test of statistical isotropy by investigating the presence of hemispherical asymmetries in our data. We find a dipole in the clustering variance of the data in the same direction ($(l, b) \sim (310°, 5°)$) as previous studies. The amplitude of this dipole is, nevertheless, in perfect agreement with the variance expected within ΛCDM.

Testing the validity of the CP is a necessary step before using any cosmological probe that, implicitly or explicitly assumes this validity. The observational evidence backing the large-scale homogeneity and isotropy of the matter distribution has grown significantly in the last few decades, and our results certainly support this evidence in the local Universe. In the near future it will be possible to impose further constraints on possible departures from the CP by performing this kind of analyses on deeper wide-area surveys. We plan to apply our methodology to the forthcoming WISE-based photometric catalogues probing 75% of the sky at redshifts $z < 0.5$ (Bilicki et al. 2014, Bilicki et al. 2015, in prep.), as well as to the Dark Energy Survey data (Flaugher 2005) covering less of the sky but at larger depths.

ACKNOWLEDGMENTS

We would like to thank Pedro Ferreira, Sigurd Næss and John Peacock for useful comments and discussions, as well as the anonymous journal referee for their insightful comments. DA is supported by ERC grant 259505. MB acknowledges the financial assistance of the South African National Research Foundation (NRF), as well as of the Polish National Science Centre under contract #UMO-2012/07/D/ST9/02785. We acknowledge the effort made by the Wide Field Astronomy Unit at the Institute for Astronomy, Edinburgh in archiving the 2MPZ catalogue, which can be accessed at `http://surveys.roe.ac.uk/ssa/TWOMPZ`.

REFERENCES

Afshordi N., Loh Y.-S., Strauss M. A., 2004, Phys. Rev. D, 69, 083524, arXiv:astro-ph/0308260
Ahn C. P. et al., 2012, ApJS, 203, 21, arXiv:1207.7137
Akrami Y., Fantaye Y., Shafieloo A., Eriksen H. K., Hansen F. K., Banday A. J., Górski K. M., 2014, ApJ. Lett., 784, L42, arXiv:1402.0870
Alonso D., 2012, ArXiv e-prints, arXiv:1210.1833
Alonso D., Bueno Belloso A., Sánchez F. J., García-Bellido J., Sánchez E., 2014, MNRAS, 440, 10, arXiv:1312.0861
Appleby S., Shafieloo A., 2014, JCAP, 10, 70, arXiv:1405.4595
Bagla J., Yadav J., Seshadri T., 2007, Mon.Not.Roy.Astron.Soc., 390, 829, arXiv:0712.2905
Beutler F. et al., 2011, MNRAS, 416, 3017, arXiv:1106.3366
Bilicki M., Chodorowski M., Jarrett T., Mamon G. A., 2011, ApJ, 741, 31, arXiv:1102.4356
Bilicki M., Jarrett T. H., Peacock J. A., Cluver M. E., Steward L., 2014, ApJS, 210, 9, arXiv:1311.5246
Bilicki M., Peacock J. A., Jarrett T. H., Cluver M. E., Steward L., 2014, ArXiv e-prints, arXiv:1408.0799
Blake C. et al., 2011, MNRAS, 415, 2892, arXiv:1105.2862
Castagnoli C., Provenzale A., 1991, A&A, 246, 634
Chon G., Challinor A., Prunet S., Hivon E., Szapudi I., 2004, MNRAS, 350, 914, arXiv:astro-ph/0303414
Coles P., Jones B., 1991, MNRAS, 248, 1
Collister A. A., Lahav O., 2004, PASP, 116, 345, arXiv:astro-ph/0311058
Crocce M., Cabré A., Gaztañaga E., 2011, MNRAS, 414, 329, arXiv:1004.4640
Durrer R., 2011, Royal Society of London Philosophical Transactions Series A, 369, 5102, arXiv:1103.5331
Durrer R., Eckmann J.-P., Sylos Labini F., Montuori M., Pietronero L., 1997, EPL (Europhysics Letters), 40, 491, arXiv:astro-ph/9702116
Eriksen H. K., Banday A. J., Górski K. M., Hansen F. K., Lilje P. B., 2007, ApJ. Lett., 660, L81, arXiv:astro-ph/0701089
Fernández-Cobos R., Vielva P., Pietrobon D., Balbi A., Martínez-González E., Barreiro R. B., 2014, MNRAS, 441, 2392, arXiv:1312.0275
Fixsen D. J., Cheng E. S., Gales J. M., Mather J. C., Shafer R. A., Wright E. L., 1996, ApJ, 473, 576, arXiv:astro-ph/9605054
Flaugher B., 2005, Int.J.Mod.Phys., A20, 3121
Francis C. L., Peacock J. A., 2010, MNRAS, 406, 2, arXiv:0909.2494
Frith W. J., Outram P. J., Shanks T., 2005, MNRAS, 364, 593, arXiv:astro-ph/0507215
Gibelyou C., Huterer D., 2012, MNRAS, 427, 1994, arXiv:1205.6476
Górski K. M., Hivon E., Banday A. J., Wandelt B. D., Hansen F. K., Reinecke M., Bartelmann M., 2005, ApJ, 622, 759, arXiv:astro-ph/0409513
Guzzo L., 1997, New Astron., 2, 517, arXiv:astro-ph/9711206
Hambly N. C. et al., 2001, MNRAS, 326, 1279, arXiv:astro-ph/0108286
Hartlap J., Simon P., Schneider P., 2007, A&A, 464, 399, arXiv:astro-ph/0608064
Hirata C. M., 2009, JCAP, 9, 11, arXiv:0907.0703
Hoftuft J., Eriksen H. K., Banday A. J., Górski K. M., Hansen F. K., Lilje P. B., 2009, ApJ, 699, 985, arXiv:0903.1229
Hogg D. W., Eisenstein D. J., Blanton M. R., Bahcall N. A., Brinkmann J., Gunn J. E., Schneider D. P., 2005, ApJ, 624, 54, arXiv:astro-ph/0411197
Huchra J. P. et al., 2012, ApJS, 199, 26, arXiv:1108.0669
Itoh Y., Yahata K., Takada M., 2010, Phys. Rev. D, 82, 043530, arXiv:0912.1460
Jarrett T., 2004, PASA, 21, 396, arXiv:astro-ph/0405069
Jarrett T. H., Chester T., Cutri R., Schneider S., Skrut-

skie M., Huchra J. P., 2000, AJ, 119, 2498, arXiv:astro-ph/0004318
Joyce M., Montuori M., Labini F. S., 1999, ApJ. Lett., 514, L5, arXiv:astro-ph/9901290
Joyce M., Sylos Labini F., Gabrielli A., Montuori M., Pietronero L., 2005, A&A, 443, 11, arXiv:astro-ph/0501583
Keenan R. C., Barger A. J., Cowie L. L., Wang W.-H., Wold I., Trouille L., 2012, ApJ, 754, 131, arXiv:1207.1588
Keenan R. C., Trouille L., Barger A. J., Cowie L. L., Wang W.-H., 2010, ApJS, 186, 94, arXiv:0912.3090
Kitaura F.-S., Jasche J., Metcalf R. B., 2010, MNRAS, 403, 589, arXiv:0911.1407
Kurokawa T., Morikawa M., Mouri H., 2001, A&A, 370, 358
Landy S. D., Szalay A. S., 1993, ApJ, 412, 64
Lewis A., Challinor A., Lasenby A., 2000, ApJ, 538, 473, arXiv:astro-ph/9911177
Limber D. N., 1953, ApJ, 117, 134
Maller A. H., McIntosh D. H., Katz N., Weinberg M. D., 2003, ApJ. Lett., 598, L1, arXiv:astro-ph/0303592
Maller A. H., McIntosh D. H., Katz N., Weinberg M. D., 2005, ApJ, 619, 147, arXiv:astro-ph/0304005
Martínez V., Saar E., 2002, Statistics of the galaxy distribution. CRC Press
Nadathur S., 2013, MNRAS, 434, 398, arXiv:1306.1700
Pan J., Coles P., 2000, MNRAS, 318, L51, arXiv:astro-ph/0008240
Park C.-G., 2004, MNRAS, 349, 313, arXiv:astro-ph/0307469
Peebles P., 1980, The Large-Scale Structure of the Universe. Princeton University Press
Peebles P., 1993, Principles of Physical cosmology. Princeton University Press
Planck Collaboration et al., 2014a, A&A, 571, A16, arXiv:1303.5076
Planck Collaboration et al., 2014b, A&A, 571, A23, arXiv:1303.5083
Pullen A. R., Hirata C. M., 2010, JCAP, 5, 27, arXiv:1003.0673
Quartin M., Notari A., 2015, JCAP, 1, 8, arXiv:1408.5792
Räsänen S., 2011, Classical and Quantum Gravity, 28, 164008, arXiv:1102.0408
Sandage A., Tammann G. A., Hardy E., 1972, ApJ, 172, 253
Sarkar P., Yadav J., Pandey B., Bharadwaj S., 2009, MNRAS, 399, L128, arXiv:0906.3431
Schlegel D. J., Finkbeiner D. P., Davis M., 1998, ApJ, 500, 525, arXiv:astro-ph/9710327
Scrimgeour M. I. et al., 2012, MNRAS, 425, 116, arXiv:1205.6812
Seshadri T. R., 2005, Bulletin of the Astronomical Society of India, 33, 1
Skrutskie M. F., et al., 2006, ApJ, 131, 1163
Sylos Labini F., 2011a, Classical and Quantum Gravity, 28, 164003, arXiv:1103.5974
Sylos Labini F., 2011b, EPL (Europhysics Letters), 96, 59001, arXiv:1110.4041
Sylos Labini F., Tekhanovich D., Baryshev Y. V., 2014, JCAP, 7, 35, arXiv:1406.5899
White M., Tinker J. L., McBride C. K., 2014, MNRAS, 437, 2594, arXiv:1309.5532
Wright E. L. et al., 2010, AJ, 140, 1868, arXiv:1008.0031
Xu X., Cuesta A. J., Padmanabhan N., Eisenstein D. J., McBride C. K., 2013, MNRAS, 431, 2834, arXiv:1206.6732
Yadav J. K., Bagla J. S., Khandai N., 2010, MNRAS, 405, 2009, arXiv:1001.0617
Yoon M., Huterer D., Gibelyou C., Kovács A., Szapudi I., 2014, MNRAS, 445, L60, arXiv:1406.1187

APPENDIX A: MOCK ΛCDM CATALOGUES

The possible deviations with respect to statistical homogeneity explored in this paper must be evaluated in terms of the statistical uncertainties already allowed by the presence of clustering anisotropies in the standard cosmological model. Although there exist analytical approximations to calculate these uncertainties (Crocce et al. 2011; Xu et al. 2013), the most reliable method to estimate them in the presence of practical complications, such as the complex sky coverage of our sample, is to use large ensembles of independent mock catalogues reproducing the expected statistical behaviour of our data. These ensembles should mimic the properties of the galaxy sample under analysis and cover a similar volume. To our knowledge, no public simulations exist with the volume of 2MASS and a sufficiently small mass resolution ($M_{\rm halo} \sim 10^{11} M_\odot/h$), and even if they did, at least $\mathcal{O}(100)$ of them would be needed in order to obtain reliable estimates of the uncertainties.

A historically popular alternative method is to generate lognormal realizations of the galaxy density field and Poisson-sample them with galaxies (Beutler et al. 2011; Blake et al. 2011). The lognormal distribution has been advocated as a possible model to describe the distribution of the non-linear matter density in the Universe (Coles & Jones 1991), and, since it is based on locally transforming a Gaussian random field, it can be used to generate large numbers of fast independent realizations. Due to its simplicity it is easy to guarantee that the mock realizations will reproduce the input power spectrum with a very good accuracy (White et al. 2014), however its validity must be carefully assessed on non-linear scales (Kitaura et al. 2010).

Although this method has been traditionally used to generate three-dimensional realizations, we have adapted it to use only angular information, using an approach similar to that of Francis & Peacock (2010). Starting from a map of the angular overdensity field in our data $\delta_d(\hat{\mathbf{n}})$, computed as described in Section 3.3, the steps used to generate each full realization are:

(i) Interpreting $\delta_d(\hat{\mathbf{n}})$ as the lognormal counterpart of an underlying Gaussian field $\delta_{G,d}(\hat{\mathbf{n}})$, we invert the lognormal transformation as

$$\delta_{G,d} = \log\left[(1+\delta_d)\sqrt{1+\sigma_d^2}\right], \qquad \text{(A1)}$$

where σ_d^2 is the variance of δ_d.

(ii) We compute the power spectrum of the Gaussian density and find its best-fit bias as explained in Section 3.3, finding the values listed in the last column of Table 1.

(iii) We generate a Gaussian realization δ_G of the best-fit theoretical power spectrum using the HEALPix routine `synfast`.

(iv) The corresponding log-normal density field is computed as

$$1 + \delta_{LN} = \exp\left[\delta_G - \sigma_G^2/2\right], \tag{A2}$$

where $\sigma_G^2 \equiv \langle \delta_G^2 \rangle$.
(v) A discrete number of galaxies are then assigned to each pixel by Poisson-sampling the lognormal field with a mean:

$$N(\hat{\mathbf{n}}) = \bar{N}\,\left[1 + \delta_{LN}(\hat{\mathbf{n}})\right], \tag{A3}$$

where $\bar{N}$ is the mean number of galaxies per pixel in the data. These mock galaxies are then distributed at random inside each pixel.

We find that this method is able to generate mock catalogues that recover the best-fit cosmological power spectrum to excellent precision on linear scales. However care must be taken when using them on small scales, where, as noted by White et al. (2014), they may not be able to reproduce the higher-order correlations of the density field. The second panel in Figure B1 shows the Mollweide projection of one of these realizations corresponding to our fiducial sample.

APPENDIX B: MOCK FRACTAL CATALOGUES

The fractal β-model (Castagnoli & Provenzale 1991) describes a multiplicative cascading process that is easy to simulate for any fractal dimension $D \leqslant 3$. We generated mock realizations of this model with dimensions $D = 2.5$, 2.75 and 2.90 using the following method:

(i) We divide a cubic box of size L, corresponding to twice the maximum comoving distance covered by 2MPZ ($\chi_{\rm max} \sim 850\,{\rm Mpc}/h$), into 8 sub-boxes by dividing each axis in half.
(ii) We give each sub-box a probability p of surviving to the next iteration, and we select the survivor sub-boxes at random according to that value of p. The value of p is related to the desired fractal dimension through

$$D = 3 + \log_2 p. \tag{B1}$$

(iii) We repeat the two previous steps on the surviving sub-boxes of the previous generation, until we reach the desired resolution.
(iv) We place one object at random inside each surviving box in the final set, and assign a K_s-band luminosity to each of these objects using the luminosity function for 2MASS measured by Appleby & Shafieloo (2014). This consists of a Schechter function with characteristic absolute magnitude $M_* - 5\log h \simeq -23.5$ and power law index $\alpha \simeq -1.02$.
(v) In terms of this absolute magnitude M_K, each object is assigned an apparent K_s magnitude in terms of its distance d to the observer, located at the centre of the box:

$$K_s = M_K + 5\log_{10}\left(\frac{d}{1\,{\rm Mpc}}\right) + 25. \tag{B2}$$

Only objects with magnitude $K_s \leqslant 13.9$ are included in the final catalogue.

The third panel in Figure B1 shows an example of one of these mock realizations for $D = 2.75$. Note that we do not intend for this model to constitute a viable alternative to ΛCDM, but only to use it as a toy model to verify the validity of the methods applied to our galaxy sample. For the same reason, the fact that we use a luminosity function which was derived assuming a FRW background should not affect our final results.

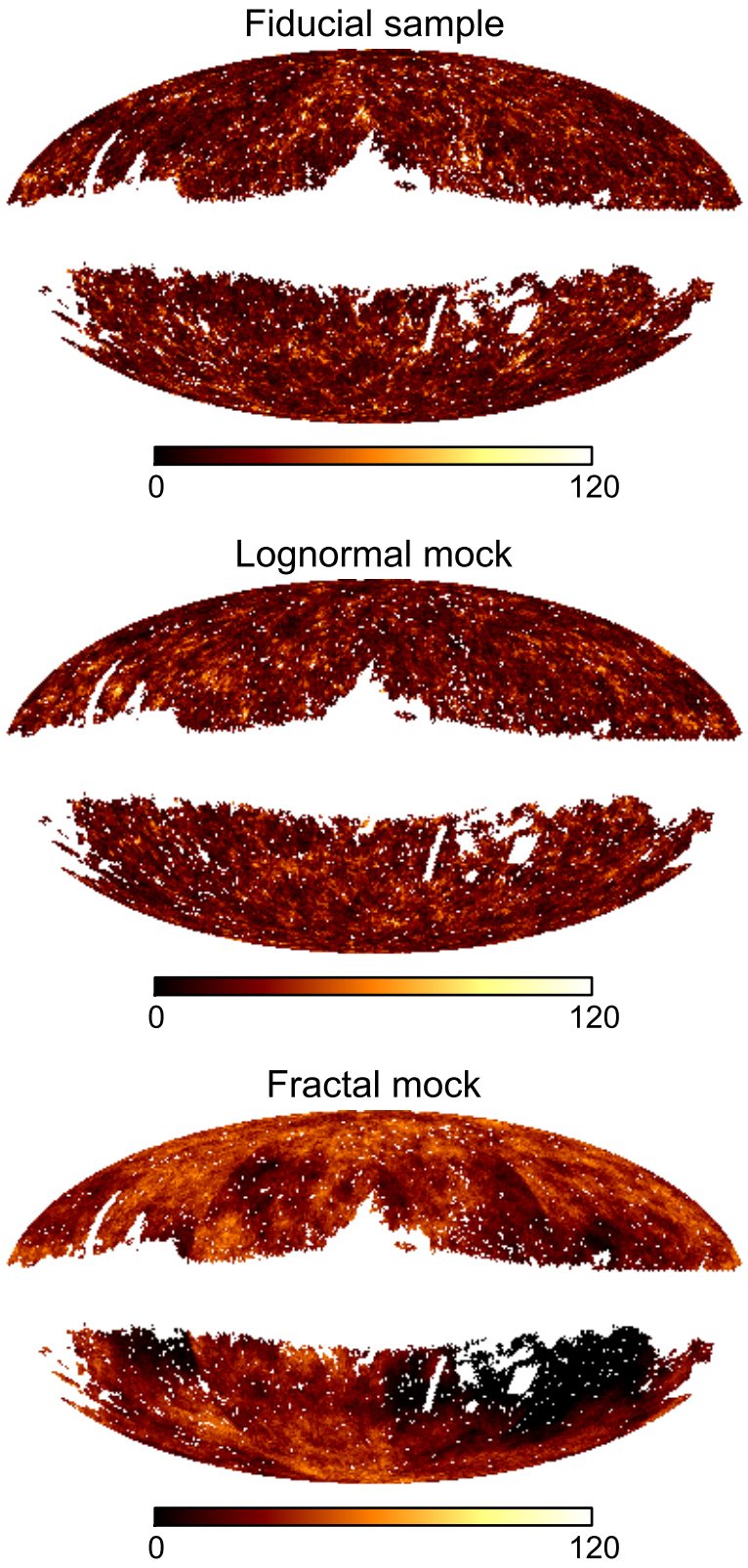

Figure B1. Number density (in $\deg^{-2}$) of objects in our fiducial sample (upper panel), for one of the lognormal realizations described in Appendix A (middle panel) and for a mock fractal realization with $D = 2.75$ (lower panel).